NRC Publications Archive
Archives des publications du CNRC

Gradient-interpenetrating polymer networks in 3D printed lattices for tunable and enhanced energy absorption

Sampson, Kathleen L.; Li, Hao; Laqua, Kurtis; Aranguren Van Egmond, Derek; Dickson, Laura E.; Barroeta Robles, Julieta; Lamouche, Justin; Guthrie, Aria; Ashrafi, Behnam; Zou, Shan; Chen, Maohui; Bell, Joshua; Paquet, Chantal

This publication could be one of several versions: author's original, accepted manuscript or the publisher's version. / La version de cette publication peut être l'une des suivantes : la version prépublication de l'auteur, la version acceptée du manuscrit ou la version de l'éditeur.
For the publisher's version, please access the DOI link below./ Pour consulter la version de l'éditeur, utilisez le lien DOI ci-dessous.

Publisher's version / Version de l'éditeur:
https://doi.org/10.1002/admt.202400403
Advanced Materials Technologies, 2024-07-12

NRC Publications Archive Record / Notice des Archives des publications du CNRC :
https://nrc-publications.canada.ca/eng/view/object/?id=92a6e78f-5b5c-4977-8463-970e9870fa1c
https://publications-cnrc.canada.ca/fra/voir/objet/?id=92a6e78f-5b5c-4977-8463-970e9870fa1c

Access and use of this website and the material on it are subject to the Terms and Conditions set forth at
https://nrc-publications.canada.ca/eng/copyright
READ THESE TERMS AND CONDITIONS CAREFULLY BEFORE USING THIS WEBSITE.

L'accès à ce site Web et l'utilisation de son contenu sont assujettis aux conditions présentées dans le site
https://publications-cnrc.canada.ca/fra/droits
LISEZ CES CONDITIONS ATTENTIVEMENT AVANT D'UTILISER CE SITE WEB.

Questions? Contact the NRC Publications Archive team at
PublicationsArchive-ArchivesPublications@nrc-cnrc.gc.ca. If you wish to email the authors directly, please see the first page of the publication for their contact information.

Vous avez des questions? Nous pouvons vous aider. Pour communiquer directement avec un auteur, consultez la première page de la revue dans laquelle son article a été publié afin de trouver ses coordonnées. Si vous n'arrivez pas à les repérer, communiquez avec nous à PublicationsArchive-ArchivesPublications@nrc-cnrc.gc.ca.

National Research Council Canada
Conseil national de recherches Canada

Gradient-Interpenetrating Polymer Networks in 3D Printed Lattices for Tunable and Enhanced Energy Absorption

Kathleen L. Sampson, Hao Li, Kurtis Laqua, Derek Aranguren van Egmond, Laura E. Dickson, Julieta Barroeta Robles, Justin Lamouche, Aria Guthrie, Behnam Ashrafi, Shan Zou, Maohui Chen, Joshua Bell, and Chantal Paquet**

3D printing provides the potential to enhance mechanical properties by fabricating complex structures with diverse materials; however, most high-resolution 3D printing techniques require custom printers to incorporate multiple materials and/or result in poor material interfacial bonding. Here, energy absorption properties are enhanced with 3D lattice structures fabricated via vat photopolymerization comprising multiple materials forming a gradient-interpenetrating polymer network (gradient-IPN). The gradient-IPN is incorporated by swelling the 3D printed elastomeric lattice in a photoresin that yields a stiff shell-soft core structure. This straightforward post-3D printing technique delivers an unprecedented degree of structural property customization through polymer gradients in lattice struts with shells of tunable stiffness and flexible elastomeric cores to achieve a broad continuum spectrum of mechanical properties within one simple system. The gradient aids in the distribution of stress and limits fracture between materials typically observed in multimaterial lattices. The gradient-IPN lattices are fully recoverable and exhibit over 4 to 33 times higher toughness after compression, compared to copolymer (same composition as the gradient-IPN) or purely elastomeric lattices, respectively. This highly versatile approach to modifying 3D printed lattices yields the unique combination of load bearing capabilities with viscoelasticity desirable for high performance materials in impact protection.

1. Introduction

3D printing has become a powerful technique to produce intricate geometries with a diverse range of materials.[1–3] In particular, 3D printing has been used to create spatially efficient energy-absorbing structures in the pursuit of fabricating light-weight materials with high toughness and energy absorption capacity together with high stiffness and strength.[4–6] The advent of 3D printing technologies has provided unique control over both material composition and structure resulting in unprecedented tuning of mechanical properties. For example, 3D printed lattices are light in weight, have intricate designs with a wide range of design freedom, are more feasible to fabricate using layer-by-layer 3D printing techniques compared to traditional methods (e.g., injection molding), and have tunable properties through both the material and structure design.[7–10] These lattices have been used as lightweight energy-absorbing materials in protective equipment in sports,[11,12] military,[13,14] and automotive industries.[15] However, the majority of research has been focused on their geometric design as opposed to novel material development, such as incorporating gradients in materials.[12,16–18] Inspired by nature, bio-inspired designs with functionally graded materials have been created to develop high-toughness and high-strength materials. These types of designs

---

K. L. Sampson, H. Li, L. E. Dickson, J. Bell, C. Paquet
Security and Disruptive Technologies Research Centre
National Research Council Canada
100 Sussex Drive, Ottawa, Ontario K1N 5A2, Canada
E-mail: kathleen.sampson@nrc-cnrc.gc.ca;
chantal.paquet@nrc-cnrc.gc.ca

The ORCID identification number(s) for the author(s) of this article can be found under https://doi.org/10.1002/admt.202400403

DOI: 10.1002/admt.202400403

K. Laqua, D. Aranguren van Egmond
Advanced Materials Research Facility, Energy, Mining and Environment Research Centre
National Research Council Canada
2620 Speakman Drive, Mississauga, Ontario L5K 1B4, Canada

J. Barroeta Robles, J. Lamouche, A. Guthrie, B. Ashrafi
Aerospace Research Centre
National Research Council Canada
2107 chemin de la Polytechnique
Montréal, Quebec H3T 1J4, Canada

S. Zou, M. Chen
Metrology Research Centre
National Research Council Canada
100 Sussex Drive, Ottawa, Ontario K1N 5A2, Canada

are found in bones and nacre in shells, in which the combination of two or more different constituent material properties work together and overcome the typical mutual exclusivity of toughness and strength.[19–21] The majority of high-resolution 3D printing techniques are better suited to forming objects with a singular material, making it challenging to introduce gradients that could reliably improve mechanical properties. Recently, 3D-printed core–shell structures were demonstrated as a means to impart such gradients, leveraging material extrusion and material jetting techniques utilizing custom-designed nozzles that extrude two materials simultaneously into a core–shell morphology to produce multi-material parts.[22] Extrusion-based 3D printing techniques have previously been used to fabricate lattices or architected structures with both stiff and soft components for energy absorption, but the materials transitioned directly from hard to soft with weak interfacial adhesion.[7,23,24] The poor interfacial bonding between the two disparate materials led to rapid crack propagation, flaking, and fracturing upon prolonged loading.[7,23,24] In contrast, vat photopolymerization 3D printing is a more desirable technique as it enables the fabrication of objects with faster speeds, smaller feature sizes, and more complex geometries than material extrusion techniques, therefore allowing a wider range of part design and material properties through the lattice architecture and polymer chemistry. While vat photopolymerization is typically limited to singular photoresins and material compositions, various new methods have been in development to expand the technique toward multimaterial 3D printing.[3,25–27]

Interpenetrating polymer networks (IPNs) are two or more distinct polymers that are molecularly intertwined, but not covalently bound, and have shown to be a successful approach to improve mechanical properties of polymer systems.[20,28] For 3D printing in particular, IPNs have been used to enhance toughness and elasticity in biocompatible hydrogels to mimic properties found in soft living tissues by including a secondary linear polymer into a photo-crosslinked polymer network.[29–31] However, these studies produced materials of very low modulus, which often led to poor resolution of parts and limited the creation of IPNs to very simple geometric structures due to the soft nature of the hydrogel and an inability for it to hold its shape. Furthermore, previous work has only delivered 3D objects consisting entirely of the IPN (no gradient). The IPN methodology has yet to be applied to the area of energy-absorbing materials for protective equipment, particularly with incorporating polymer gradients. Gradient-IPNs have been found to have significantly improved mechanical properties compared to homopolymers or non-gradient-IPNs, due to stresses being distributed over a progressive change in the polymer network. The gradient-IPN morphology imparts global properties that emerge from the combination of stiff and soft regions, together resulting in a trend toward prolonged plastic deformation instead of brittle fracture.[32] The beneficial properties of gradient-IPNs, as shown with 2D materials or films, have been found to be more evident when gradient-IPN polymer components have large differences in mechanical properties, i.e. hard and soft.[32] The gradient in polymers affords a gradual variation in material properties between those extremes, thereby preventing interfacial failure. In this work, we introduce a robust and universal approach to fabricate gradient-IPNs within elastomeric, 3D-printed lattice materials during a post-printing step, imparting both high toughness and strength to architected structures for protective applications. This is achieved in a simple system of two polymers, individually unfavorable for energy absorption, using a precisely tunable framework that alters the morphology of gradient-IPNs within an existing 3D printed geometry. An intentional gradient in polymers is created, whereby the cross-sections of the lattice struts gradually transition from a region of stiff IPN to soft elastomer, resulting in a novel stiff shell-soft core morphology throughout the lattice structure (**Figure 1a**). With our approach, we show how to further combination with complex geometries and structural design enables the beneficial properties of a gradient-IPN to drastically enhance and customize the energy absorption behavior of 3D printed lattices for advanced protective structures.

Our approach offers many key advantages. First, this method is simple, scalable, cost-effective, and applicable to many distinct polymer systems. It involves steps already commonly used to post-process 3D printed parts from vat photopolymerization printers (i.e., soak, dry, and cure). The gradient-IPN 3D printed lattice method we developed is also highly versatile, with a number of parameters that can be altered to tune the properties. In this study, we explored variations in the types of polymers, the amount of gradient-IPN introduced, the degree of polymerization, and the type of 3D-printed lattice the gradient-IPN was applied to. Ultimately, the gradient-IPN resulted in enhanced mechanical properties of the 3D-printed lattice. The enhancements are shown to be highly tailorable and result from the interplay between lightweight lattice design principles, the core–shell morphology, and the interfacial robustness between the stiff and soft materials. Overall, we developed a method to fabricate 3D printed lattices with gradient-IPNs forming a stiff shell-soft core morphology. We showed that the morphology can be altered via polymer type, amount of IPN, and lattice structure and that enhanced energy absorption was achieved and highly tunable compared to monolithic polymer structures. The enhanced energy absorption properties of these materials will pave the way for high-performance impact protection.

2. Results and Discussion

Gradient-IPN lattices were fabricated in a simple two-step process. First, a 3D lattice, made from an elastomeric polyurethane, was printed using a digital light processing (DLP) 3D printer (Figure 1a, step 1). This was followed by swelling (infiltration) and curing of an acrylate photoresin that forms a stiff polymer within the outer layers of the polyurethane network (Figure 1a, step 2–3). The polyurethane photoresin formulation was modified from the work by Patel et al. who developed a highly stretchable, UV-curable elastomer that outperforms commercial elastomers in terms of elongation at break.[33] The modified resin consisted of a urethane-based difunctional crosslinking monomer (aliphatic urethane diacrylate, Ebecryl 8413) and two monofunctional reactive diluents (epoxy aliphatic acrylate (Ebecryl 113) and isobornyl acrylate) to adjust the viscosity for DLP printing. The photoresins used in the second step were UV-curable acrylates that could swell the polyurethane polymer to form an IPN with increased stiffness. By immersing the elastomeric 3D lattice into the liquid acrylate photoresin (stiff phase precursor) for a desired time (Figure 1a, step 2), the acrylate

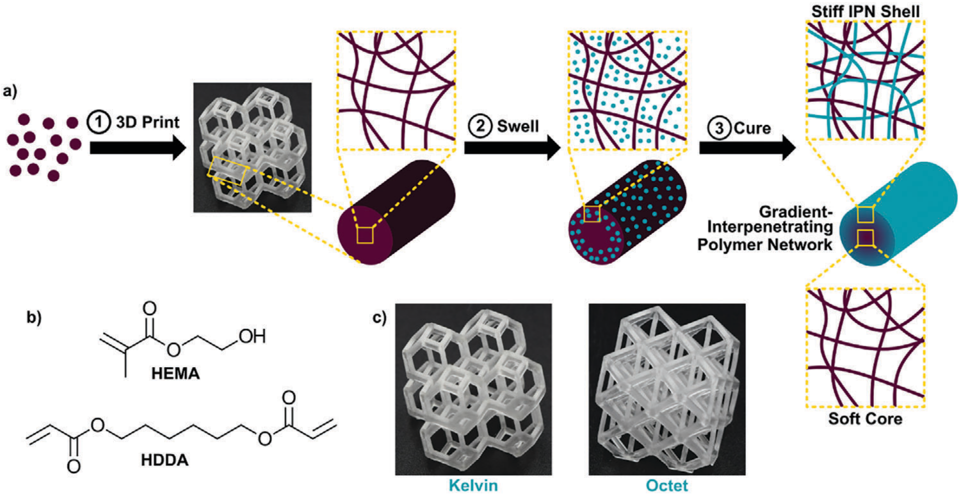

Figure 1. a) Method of forming a gradient-IPN core–shell structure within a 3D printed lattice. The soft, elastomeric lattices are 3D printed followed by swelling in a second photoresin that forms a stiff polymer. The stiff polymer photoresin is then cured in the 3D lattice using UV light. The struts within the final 3D printed lattice contain a stiff shell comprised of an IPN of the stiff polymer and elastomeric polyurethane, while the core contains only the soft elastomeric polyurethane, overall forming a gradient-IPN. b) Monomers for the stiff polymer photoresin explored in this study include 2-hydroxyethyl methacrylate (HEMA) and 1,6-hexanediol diacrylate (HDDA). c) Images of 3D printed 2 × 2 × 2 Kelvin and octet-truss based lattice structures made of polyurethane (dimensions of 24.99 × 24.99 × 24.99 mm).

photoresin diffused into the polymer network to an extent that depended on the compatibility between the polyurethane polymer and the acrylate photoresin, the size of the polyurethane polymer part (i.e., lattice strut diameter), and the swelling time. After the desired swelling time, the object was removed, dried, and the lattice was cured with UV light (Figure 1a, step 3). A stiff, interconnected network of the two types of polymers formed in the areas where diffusion occurred and gradually transitioned into the elastomeric core where no diffusion took place, without any sharp material interface. This core–shell morphology within the lattice struts is referred to as a gradient-IPN. Overall, the 3D printed lattice was imparted with a spatial gradient in the polymers and, therefore, variation in the mechanical properties throughout the cross-section of all struts in the lattice. This additional step to form the gradient-IPN can easily be implemented as it is similar to typical post-printing steps (wash, dry, post-cure) and can be applied to lattices with diverse sizes and shapes for a variety of applications, such as sporting goods, automotive parts, and vibration canceling devices.

In this work, the mechanical properties of lattices were systematically tuned and augmented with the gradient-IPN lattice morphology by altering three parameters: 1) the types of stiff reinforcing polymers used, 2) the extent of swelling, and 3) the lattice geometry. The polymer material composing the core was kept constant (elastomeric polyurethane), while the stiff polymer comprised of either a monofunctional acrylate, 2-hydroxyethyl methacrylate (HEMA), or a difunctional acrylate crosslinker, 1,6-hexanediol diacrylate (HDDA) (Figure 1b). HEMA as the secondary polymer has one acrylate polymerizable group and forms a linear chain and has been used previously to form a gradient-IPN with thermal curable polyurethane.[34] This is contrary to HDDA, which has two acrylate polymerizable groups and forms a very stiff, highly crosslinked 3D network.

The core–shell morphology in the gradient-IPN lattice struts was characterized by two methods: fluorescence microscopy of samples prepared with the stiff polymer photoresins containing a fluorescent dye (fluorescein isothiocyanate, FITC) and comparing changes in weight and dimensions before and after forming the gradient-IPN. The cross-sectional images of the cured gradient-IPN samples were marked by fluorescent areas where the dye-doped stiff polymer diffused into the polyurethane network and dark areas (i.e., the core) that were composed of only the polyurethane elastomer (**Figure** 2a). The images were used to calculate a percent diffusion, which represents the length of diffusion of the stiff polymer into the test object relative to the thickness of the swelled gradient-IPN sample. The percent diffusion length of HEMA was 14%, 24%, and 39%, while for HDDA it was 17%, 25%, and 36% after 5, 15, and 60 min of swelling time, respectively. This illustrated that the thickness of the stiff IPN shell can be controlled by tuning the swelling times (Figure 2b). After two days of swelling (2880 min), the cross-sections were completely fluorescent, indicating the stiff polymer photoresin had fully penetrated the rods (non-gradient-IPN, Figure S1, Supporting Information). When monitoring the change in weight of cylindrical polyurethane rods with a nominal diameter of 1.25 mm (same diameter as the individual lattice strut diameter used below), similar trends were observed, particularly when compared to the percent diffusion measurements from fluorescence microscopy images. The formation of the HEMA and HDDA gradient-IPNs both led to the expansion in length and diameter of the rods with increasing swelling time (Figure 2c-d). This correlated with the increase in weight (wt.%), which converged toward a maximum ≈62 wt.% HEMA and ≈70 wt.% HDDA after three days of swelling (Figure 2e). HDDA had slightly higher changes in size and weight due to the faster diffusion of HDDA into the polyurethane network compared to HEMA. It is theorized that the hydroxy group of the HEMA and possible

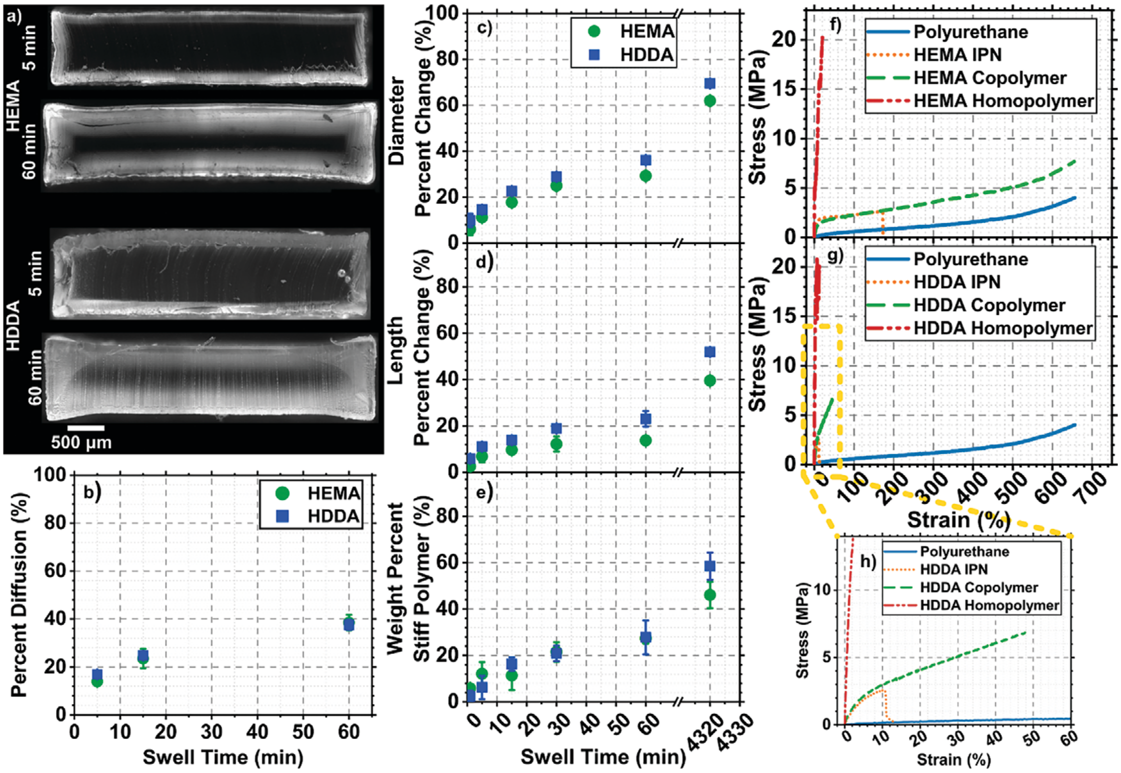

Figure 2. a) Fluorescence microscopy images of the cross-sections of gradient-IPN rods with HEMA and HDDA as the stiff polymer, showing increasing thickness of the IPN stiff shell with increasing swelling time of 5 or 60 min. b) Percent diffusion of HEMA (green circles) and HDDA (blue squares) into polyurethane rods calculated from the thickness of the fluorescent dye labeled IPN shell as a function of swelling time from fluorescence microscopy images. c) Percent change in dimensions of gradient-IPN rods compared to the original polyurethane rods in terms of c) diameter and d) length with increasing swelling time in HEMA (green circles) and HDDA (blue squares) stiff polymers. e) Change in weight percent (wt.%) of rods with HEMA (green circles) and HDDA (blue squares) stiff polymers in the IPN as a function of swelling time. Stress–strain curves from tensile tests of rods comparing polyurethane (blue solid line), gradient-IPN (orange dotted line), copolymer (green dashed line), and a homopolymer (red dashed and dotted line) of the stiff polymer, where the gradient-IPN, copolymers, and homopolymers are composed of f) HEMA and g) HDDA as the stiff polymer. h) Zoomed-in depiction of the stress–strain curves from tensile tests of rods containing polyurethane (blue solid line), HDDA IPN (orange dotted line), HDDA copolymer (green dashed line), and an HDDA homopolymer (red dashed and dotted line), highlighting the additional drop in stress associated with the HDDA IPN shell breaking followed by the polyurethane core in the HDDA IPN curve.

hydrogen bonding with the polyurethane network slows the diffusion of HEMA compared to HDDA, but this is being further investigated in a separate study. Overall, 6.02 ± 2.56 wt.% HEMA and 9.94 ± 2.85 wt.% HDDA were achieved in as little as 1 min swelling with highs of 61.93 ± 0.11 wt.% HEMA and 69.49 ± 0.30 wt.% HDDA observed with three days (4320 min) of swelling. When rods with different nominal diameters (1.00, 1.25, 1.50, 1.75, and 2.00 mm) were swelled for a constant time of 15 min in HEMA and HDDA, the relative fraction of HEMA and HDDA incorporated into the rods decreased with increasing rod diameter (Figure S2, Supporting Information). While the extent of swelling with the stiff polymer photoresin and overall thickness of the IPN shell remained similar between samples, rods with larger diameters yielded a smaller ratio of IPN shell thickness to the polyurethane core and, therefore, had an overall lower weight fraction of the stiff polymer in the gradient-IPN. Fourier transform infrared spectroscopy (FT-IR) and differential scanning calorimetry (DSC) were also performed on the homopolymers, copolymers, and IPN materials to verify the polymer conversion and glass transitions (Tg) for each composition (Figure S24 and Table S11, Supporting Information). FT-IR results demonstrate high polymer conversions after printing and post-processing while the DSC results show the IPNs have two glass transitions temperatures, which suggests a core–shell morphology forms. These results demonstrate how the type of stiff polymer (linear or crosslinked polymer) and the thickness of the IPN shell can easily be tuned by rational selection of the photoresin type and by varying its swelling time in order to yield control over the composition and morphology of the final lattice struts.

Cylindrical rods with nominal diameters of 1.25 mm underwent quasi-static tensile tests in order to establish the baseline mechanical properties of the constituent materials in the lattices without the complex loading of the lattice structures (Figure 2f–h; Figure S3 and Table S1, Supporting Information). Uniaxial tensile testing was used as a baseline comparison between the different polymer morphologies and materials. Tensile tests were chosen to represent a "worst-case" loading scenario for the gradient-IPN materials, as they produce a uniform stress profile across the sample cross-section (this contrasts the compression tests in later sections, which were performed on the lattice structures fully integrated with the gradient-IPN and are influenced by both the material and geometric structural design). In tensile testing, the effect of microstructural defects (e.g., microvoids, interfacial mismatch, etc.) is amplified, allowing us to study the tensile resilience of the entire cross-section experiencing pure failure. Rods made of copolymers of the constituent monomers of the core and shell materials were 3D printed and tested alongside the gradient-IPNs to determine if changes in mechanical properties were due to the gradient-IPN core–shell morphology or only the compositional effect of introducing HEMA or HDDA. The copolymers were prepared using the monomers of the polyurethane polymer and stiff HEMA or HDDA polymer in a similar weight ratio to those in the gradient-IPN (see Table S3, Supporting Information for the compositions of the copolymers and gradient-IPNs tensile test samples), yielding 3D printed cylindrical rods with similar polymer compositions as the gradient-IPNs, but with spatially uniform (non-IPN) morphologies. Therefore, the mechanical properties from the gradient-IPN core–shell morphology can be directly compared to a copolymer analog under uniform tensile stress without confounding the effects of the materials with those arising due to the structure of a 3D lattice.

As expected, the HDDA and HEMA homopolymers were very brittle with high modulus and ultimate tensile strength. On the other hand, the polyurethane homopolymer had the lowest modulus and one of the highest elongations. The mechanical properties of the IPNs and copolymers imparted various properties of both constituent materials, but were highly dependent on the morphology (i.e., core–shell gradient-IPN vs copolymer). While the mechanical properties of the copolymer rods under tensile stress appeared to be superior to the respective gradient-IPN rods (Figure S3, Supporting Information), upon closer inspection of the stress–strain curves in Figure 2f,g (highlighted in the zoomed in Figure 2h showing the HDDA IPN and analogous copolymer), the increase in toughness of the copolymer rods was predominantly attributed to their increase in overall tensile ductility (i.e., elongation). Below a certain elongation (i.e., ≈170% strain for HEMA IPN and ≈10% for HDDA IPN), there was no appreciable difference in stress–strain response between the gradient-IPN and copolymer. The stress–strain curves overlapped and the moduli were very similar (for example, the HDDA IPN modulus was 66.65 ± 12.36 MPa vs the HDDA copolymer modulus of 65.46 ± 28.37 MPa). These results indicated the stiffness of the collective soft core and stiff shell of the gradient-IPN matched that of the copolymer rods with uniform morphology. However, the elongation, and thus overall toughness, of the gradient-IPN rod was lower as a result of the stiffer shell compared to the polyurethane elastomer and the copolymer analog. This may be understood as follows: due to the large stiffness mismatch between core and shell polymers, the effective modulus and strength of the composite IPN are dominated by the shell's contribution. Under tensile stress, once a crack was able to form in the stiff shell phase and since the entire cross-section experienced the same stress (which is far above the tensile strength of the soft core polymer), the crack could propagate rapidly across the interface and through the soft core, causing complete failure. This near-instantaneous sequential fracture of the stiff shell through to the soft core can be seen in the rapid drop in stress in both the HEMA and HDDA IPN rods immediately following the ultimate tensile strength point (particularly for the HDDA IPN as shown in Figure 2h). Notably, despite having lower modulus and strength, the HEMA IPN boasted much greater elongation and toughness compared to the stiff HEMA homopolymers (single material). The stiff shell-soft core morphology formed by the gradient-IPN is similar to that of Mueller et al. where a custom coaxial printhead was used to extrude struts composed of a flexible epoxy core and brittle epoxy shell.[23] A similar result was also found by Mueller et al. whereby the combination of two or three materials resulted in a lower modulus than the monolithic brittle polymer, but an increase in the energy absorption with an optimal ratio of the three materials (core, interface, and shell).[23] This creates a fascinating opportunity for parametric optimization based on gradient-IPN variations. Overall, the tensile test results begin to illustrate how the stiff shell-soft core morphology of the gradient-IPN combines the benefits of both the stiff and soft polymers: the stiff shell improved the modulus compared to the polyurethane, while the soft core provided more elasticity compared to the stiff homopolymer. As described in subsequent sections, the forces during lattice compression are not pure tension; thus, the effect of the stiff shell and viscoelastic core was evaluated on 3D lattice structures fully integrated with a gradient-IPN under compressive energy absorption and shown to impart desirable properties for impact protection.

Architected low-density samples were fabricated with two distinct classes of 3D lattice geometry to examine the effect of gradient-IPN and lattice structure on their effective compressive behavior. In compressive loading, the individual struts of a 3D lattices undergo a variety of mechanical deformation modes depending on the strut's orientation relative to the externally applied load. Combinations of axial and lateral loads lead to flexural stresses and varied buckling behaviors unique to each strut. For this study, lattices were maintained at 1.25 mm nominal strut thickness and 2 × 2 × 2 number of unit cells in the x, y, and z direction, while the relative density (ratio of volume of struts to entire lattice volume from its outer dimensions), unit cell geometry, and primary mechanism of deformation (i.e., stretching- vs bending-dominated lattices) were altered. Stretching-dominated structures (e.g., octet lattices) result in higher modulus, initial peak strength, and overall toughness than bending-dominated lattices (e.g., Kelvin-style lattices) of the same relative density.[35] In stretching-dominated lattices, energy is primarily dissipated by axial deformation in every strut (under elastic loading), whereas struts in bending-dominated lattices are able to bend away from the strut axis, thus dissipating more energy. This is true for rigid lattices, but proves more complex in lattices made from elastomeric materials. For a purely elastomeric lattice with "stretching-dominated" geometry (e.g., octet-style), the behavior after the initial peak strength is defined by softening due to buckling of the struts. This causes a large deviation from the ideal "flat" stress–strain curve desired for energy absorbers and can therefore be less promising for impact attenuation.[35] The ideal energy absorber includes both the shape of the stress–strain curve (i.e., steep linear increase of stress up to a yield point, followed by sustained plateau stress near the magnitude of the yield stress) as well as the toughness or area under the curve. The effect of the gradient-IPN on both bending- and stretching-dominated structures was observed using two different 3D printed polyurethane lattice structures: the Kelvin lattice with a nominal relative density of 0.07 and octet truss-based

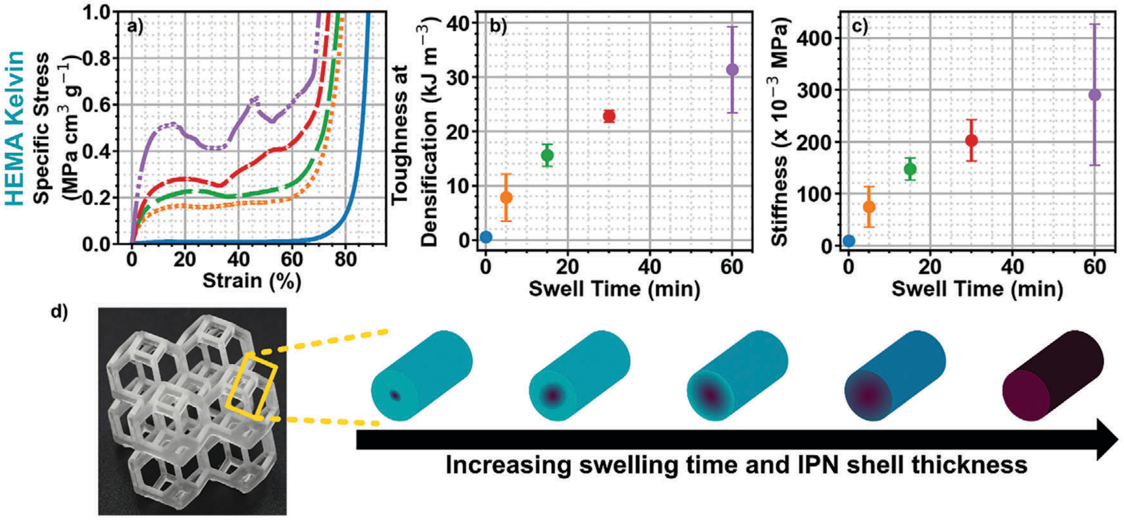

Figure 3. Effect of swelling time on mechanical properties of Kelvin lattices swelled in HEMA for 0 (polyurethane), 5, 15, 30, and 60 min, including a) specific stress–strain curves, b) toughness at densification, and c) stiffness as a function of swelling time. d) Graphical representation of the increasing IPN shell thickness increasing with swelling time for the struts in a Kelvin lattice.

lattice with a nominal relative density of 0.14 (Figure 1c). The relative densities of the Kelvin and octet lattices were different in order to maintain the same strut diameter (1.25 mm) and weight fraction of the stiff polymer in the gradient-IPN lattices between the two structures. For all compression tests, the stress was normalized to the actual measured density of the lattices (mass divided by outer lattice dimensions) and reported as specific stress, in order to account for the increase in size and mass of the lattices upon swelling and formation of the gradient-IPN. Overall, with the gradient-IPN method, the mass increased fairly linearly with the increase in dimensions (≈5% or less difference in density of the IPNs compared to polyurethane lattices, see Tables S2–S7, Supporting Information for density measurements) and did not significantly change the observed trends in mechanical properties.

The mechanical properties from compression tests of 3D printed lattices with a gradient-IPN core–shell morphology were evaluated using HEMA as the stiff polymer and different swelling times (**Figure 3**; Figures S4–S6 and Table S2, Supporting Information). The Kelvin lattices, made with the polyurethane elastomer and swelled in HEMA for 5, 15, 30, and 60 min, had increasing toughness at densification (see Experimental Section for method of calculation) with increasing swelling time. There was an over 55-fold increase in toughness with the thickest IPN shell (60 min swelling) compared to the elastomeric polyurethane lattice alone (Figure 3b). The thicker HEMA IPN shell with increasing swelling time stiffened the material and allowed for higher energy absorption (Figure 3c). Below 30 min of swelling in HEMA, the lattice responded with a flat stress–strain curve (elevated plateau stress after yield) with the ability to sustain even force under further compression. This is ideal for energy absorbers, combining the higher toughness with efficient energy absorption. With 30 min or more of swelling, the stress–strain curves displayed several subsequent peaks and drops in stress, which were a result of partial brittle “cracking” of some struts associated with the fracturing of the stiff HEMA polymer in the IPN shell. This indicated that with extensive swelling with the stiff polymer photoresin, the lattices started to progressively take on properties closer to that of the homogeneous stiff polymer (it became less core–shell in its behavior). At high swelling times (i.e., 60 min), there may be non-uniformity in the gradient-IPN thickness and curing of the stiff polymer between duplicate samples, which caused the stiff polymer to crack in different locations within the lattice between samples and led to variation in the toughness and stiffness. The increase in toughness and stiffness with a thickness of the stiff IPN shell emphasizes the high versatility of the gradient-IPN technique by showing a wide range in performance by just altering the swelling time (Figure 3d). The optimal swelling time and thickness of the IPN shell can be tuned for the desired mechanical properties and application.

The universality of this gradient-IPN method was shown by applying the same swelling times to octet lattices with the same strut diameter (1.25 mm), but higher nominal relative density (0.14) and swelled in HDDA (Figures S4–S6, and Table S2, Supporting Information). Similar to the HEMA Kelvin IPN lattices, increasing the swelling time resulted in increased toughness at densification and stiffness in addition to steeper drops in the stress–strain curves (i.e., higher occurrence of failure in the thicker stiff IPN shells). Curing conditions of the HEMA or HDDA stiff polymers were also shown to have an effect of the mechanical properties and shape of the stress–strain curve due to variations in the crosslink density and modulus of the stiff polymer (see Figure S7 and Table S3, Supporting Information for details). Optimized curing conditions for each stiff polymer were chosen from these results (constant curing at 45 °C for 60 min for HEMA and 65 °C for 60 min for HDDA). As a comparison, a Kelvin and octet lattice composed of the stiff HDDA homopolymer (100% HDDA) was 3D printed (Figure S8 and Table S4, Supporting Information) (it was not feasible to 3D print control lattices made from a HEMA homopolymer due to the lack of crosslinking (linear polymer) to support layer-by-layer fabrication). While both the Kelvin and octet HDDA homopolymer lattices had the highest absolute toughness, they were not very efficient at absorbing energy with maximum efficiencies less than 34% (compared to ≈40–47% with the HDDA IPNs) and catastrophic drops (greater than ≈50% drop) in specific stress due to the successive and complete fracturing of the brittle struts throughout the lattice. While high toughness is desirable, it must also be accompanied by an ideal "flat" shape to the stress–strain curve, low stress transferred to the object the lattice is protecting (low peak stress), and high recoverability, which the homopolymer HDDA lattices did not exhibit. Therefore, the gradient-IPN lattice results demonstrated the remarkable improvement in energy absorption that can be achieved through the 3D design of gradient-IPN lattices and synergistic properties of the core–shell structure in comparison to a uniform polymer morphology. In addition, the gradient-IPN lattices are highly versatile, with the ability to tailor their responses to compression forces through easy tuning of the fabrication parameters (polymer type, core/shell thickness ratio, and lattice design). For instance, the lattices can be designed to limit peak stress to below a desired force or, alternatively, maximize energy absorption.

The compression response of the Kelvin and octet copolymer lattices were compared to their gradient-IPN analogs to confirm the improved energy absorption properties were a result of the gradient-IPN core–shell morphology and not the incorporation of HEMA or HDDA in the polymer material (**Figure 4**; Table S5 and Figure S9, Supporting Information). To confirm the overall lattice structure does not drastically change with the gradient-IPN method, the nodes of each type of lattice and material were compared using optical microscope images (Figure S10, Supporting Information). The nodes showed even material distribution without fillet formation (thickening of the lattice edges) with the gradient-IPN method as the edges and nodes expanded proportionally with the addition of the stiff polymer. Under compression, all four gradient-IPN lattices, Kelvin and octet with HEMA and HDDA as the stiff polymer, surpassed the toughness, maximum efficiency, stiffness, and densification strains of the corresponding copolymer lattices, demonstrating their superior energy absorption capabilities. Remarkably, the octet HEMA IPN had a toughness at densification of 30.79 ± 2.09 kJ m^{-3} compared to 7.73 ± 0.22 kJ m^{-3} for the octet HEMA copolymer, both with similar wt.% HEMA in the material. The maximum energy absorption efficiency (see Experimental Section for method of calculation) reached as high as 51.14 ± 1.81 % with the octet HDDA IPN lattice. The octet HDDA IPN lattice was also over 33 times higher in toughness compared to the polyurethane. The gradient-IPN morphology also increased the densification strain allowing more capacity for energy absorption. Between the HDDA and HEMA IPN lattices, the toughness, stiffness, and initial peak stress were greater for the HDDA IPN lattices (both Kelvin and octet) than the HEMA IPN lattices due to the higher modulus of HDDA, the ability of HDDA to crosslink, as well as the higher diffusivity of HDDA for the same 15 min swelling time (higher wt.% HDDA than HEMA in lattices). Regardless of whether or not the mechanical properties are normalized to density, the trend remains the same, whereby the specific toughness and specific peak stress of the gradient-IPN lattices were higher compared to those of the copolymer analogs (Figures S11 and S12, Supporting Information). This trend was also true when the polyurethane and copolymer lattices were scaled and printed to be similar in size to the gradient-IPN lattices (Figures S13–S15, and Table S6, Supporting Information). The original conclusion remained where the gradient-IPN lattices had higher toughness due to higher stiffness and initial peak stress than the copolymer analogs with equivalent wt.% stiff polymer, for both the original sized and scaled copolymer lattices. The gradient-IPN method allows for more efficient placement of the stiff polymer near the edge (shell) of the lattice struts compared to being randomly incorporated into the copolymer, which enables the combined beneficial viscoelastic and load-bearing properties desired for enhanced energy absorption.

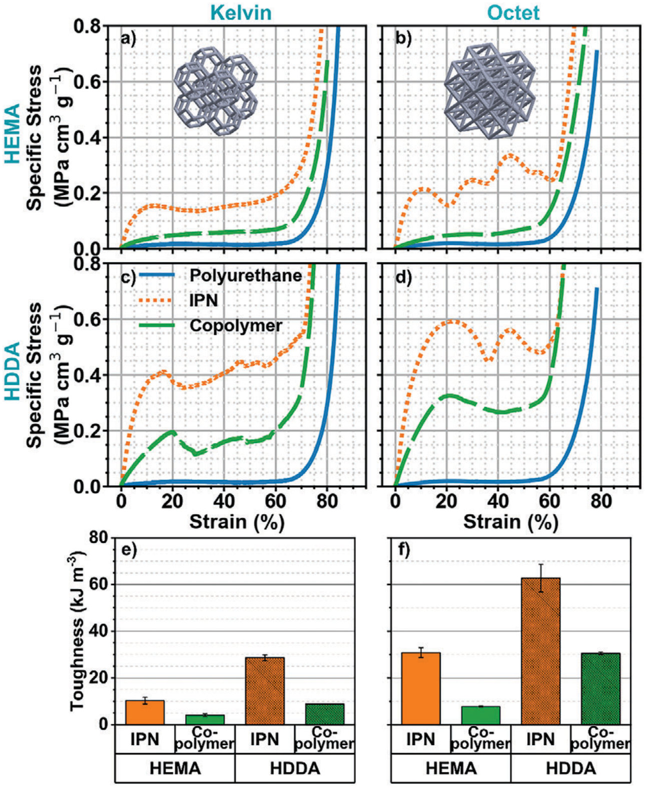

Figure 4. Compression test specific stress–strain curves and toughness at densification mechanical properties of lattices with different unit cell type and IPN stiff polymers comparing polyurethane (blue), gradient-IPN (orange), and copolymer (green) materials. The lattice parameters tested were HEMA (a and b, solid bar plots in (e) and (f)) and HDDA (c and d, hashed bar plots in (e) and (f)) as the stiff polymers swelled for 15 min and Kelvin a, c, and e) and octet b, d, and f) unit cells. Inset images in (a) and (b) are models of the Kelvin and octet lattice.

Differences between the Kelvin and octet lattices were also evaluated from the stress–strain curves, mechanical properties, and images of the deformation of the lattices during compression tests (**Figure 5**; Figures S16, and S17, Supporting Information). The octet lattices compared to Kelvin lattices had significantly higher toughness and stiffness, predominantly due to the higher nominal relative density of the octet lattice (0.14 vs 0.07, respectively) and its ability to transition from buckling to axially stretching-dominated deformation with the addition of increasing stiff phase. As mentioned previously, the nominal strut diameters of the Kelvin and octet lattices were kept the same at 1.25 mm to ensure a similar weight fraction of the stiff polymer

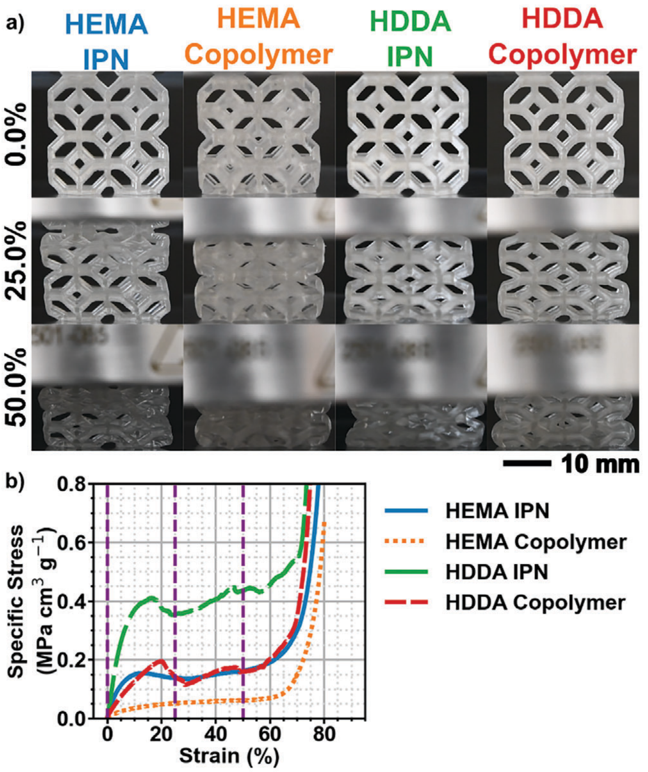

Figure 5. Video frames during compression tests of gradient-IPN and copolymer Kelvin lattices with HEMA and HDDA as the stiff polymers at 0.0, 25.0, and 50.0% strain. b) Associated specific stress–strain curves of the gradient-IPN and copolymer lattices compressed in (a)) with vertical purple dashed lines representing each video frame capture at 0.0, 25.0, and 50.0% strain.

between the two geometries, leading to different nominal relative densities. The octet IPN lattices were characterized by fluctuating peak-valley stress–strain behavior in the post-yielding region, which is typical of the stretching-dominated geometry and plastic buckling or irreversible damage of the struts (i.e., cracks in the stiff IPN shell).[35] However, a higher number and more catastrophic drops in the stress were observed with the octet IPN lattices than the respective copolymer lattices. The drops corresponded to the buckling of each half of the two unit cells, as seen in the video frames and specific stress–strain curves in Figure S17 (Supporting Information), and were due to the gradient-IPN and/or the incorporation of a stiff material into the lattice. Both the HDDA and HEMA IPN octet lattices and the HEMA IPN Kelvin lattice exhibited non-uniform deformation with one row of unit cells deforming first followed by the subsequent layer of unit cells after 25% strain (Figures S16 and S17, Supporting Information). The deformation of the HDDA IPN Kelvin lattice was more uniform with each unit cell layer compressing, but with some tilting occurring between layers at ≈37.5% strain (Figure 5). These different mechanisms of deformation with the gradient-IPN were in contrast to the copolymer lattices in which both the layers of unit cells appeared to deform under compression at the same time, regardless of the material or lattice type (Figure 5a). The gradient-IPN morphology had a significant effect on the stress distribution during compression and can be a means to control the different modes of deformation (i.e., whether a layer of lattice unit cells takes on the initial stress or the stress is evenly distributed throughout the structure).

The stress–strain responses of the cylindrical rods under tensile forces (Figure 2f–h) compared to the 3D lattices under compression forces (Figures 3 and 4) showed important differences in stress dissipation. While the tensile stress caused complete fracture once a crack formed in the stiff IPN shell, the stiff shell-soft core of the gradient-IPN was beneficial for the 3D lattice under compression as the IPN shell was sufficiently stiff to cause buckling at higher stress, but also contained the elastic core to avoid brittle fracture. The gradient-IPN lattices absorbed compressive energy at little sacrifice of the constituent material properties. The increased benefit of the stiff IPN shell during compression tests compared to tensile tests can be seen by evaluating the difference in modulus between the gradient-IPNs and their copolymer analogs under compressive forces on the 3D lattices (effective modulus) compared to under tensile force on the rods (Figures S3 and S17, Supporting Information). The gradient-IPNs exhibited a higher effective modulus than the copolymers for all compression tests (HEMA and HDDA stiff polymers and Kelvin and octet lattices). This trend was also true when considering density (specific effective modulus). This is in contrast to the similar modulus between the gradient-IPNs and copolymer analogs from tensile tests. The individual struts of the lattices during compression undergo a variety of deformation modes, which depend on the strut's orientation relative to the direction of the force. As well, the forces experienced by the lattices are not just tension. The gradient-IPN stiff shell-soft core morphology was designed for compression and was shown to significantly impact the dissipation of stress and improve energy absorption under compression of 3D lattices.

Overall, the core–shell structure led to enhanced stiffening and dissipation of energy throughout the lattices and can be easily tuned for the desired application with type of the stiff polymer material, thickness of shell, and lattice geometry. Compared to other stiff-soft 3D printed lattice materials, the gradient-IPN lattices exhibited more desirable "flat" stress–strain curves with minimal drops in stress associated with fracturing in the struts. While Yavas et al. was able to tune the stiffness and energy absorption of their hexagonal planar lattice structures with the ratio of the hard polylactic acid shell and the thermoplastic polyurethane core using an extrusion-based printer, the lattices reached a certain stress value during compression then dropped due to failure at the interface between the two materials.[24] Mueller and Shea were also able to tune the energy absorption as well as the degree of failure of their Kelvin lattices with the core–shell ratio of rigid and rubber-like photocurable materials, respectively, fabricated using a multimaterial jetting 3D printer; however, the lattices experienced drops in load due to consecutive failure at the material interfaces.[7] Both studies show how the interface between the two materials is crucial for stress transfer in energy-absorbing materials. The gradient-IPN lattices showed minimal to no failure, depending on the thickness of the IPN shell, degree of cure of the stiff polymer, and type of stiff polymer, due to the gradient in properties and blended material interface that is able to distribute the stress.

Cyclic loading-unloading compression tests were performed on Kelvin and octet lattices to evaluate the energy dissipation

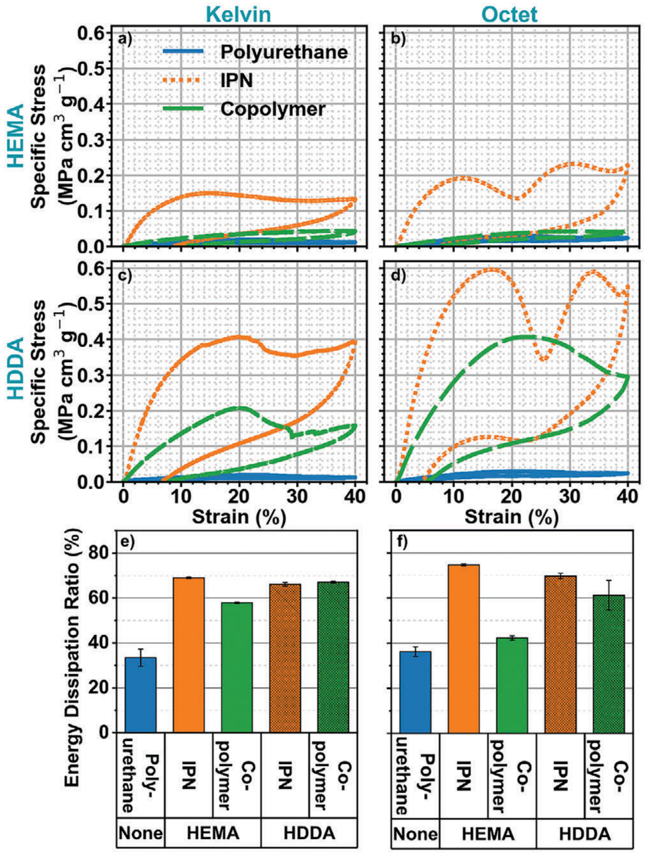

Figure 6. Cyclic compression test specific stress–strain curves and energy dissipation ratios with different lattice unit cell types and stiff polymer materials tested comparing polyurethane (blue), gradient-IPN (orange), and copolymer (green). The lattice parameters tested are HEMA (a, b, and solid bars in (e) and (f)) and HDDA (c, d and hashed bars in (e) and (f)) as the stiff polymers and Kelvin a,c, and e) and octet b,d, and f) unit cells.

and recoverability with different compositions (**Figure 6**; Figure S18, and Table S7, Supporting Information). When lattices were compressed to 40% strain at a rate of 10% strain min^{-1} and returned to the original position, the Kelvin and octet lattices made of the elastomeric polyurethane, showed minimal hysteresis loops. This is typical for elastic materials such as rubber, indicating limited energy dissipation.[36] The energy dissipation ratios were much higher for the gradient-IPN and copolymer lattices. In particular, the energy dissipation ratios of the gradient-IPN lattices surpassed those of the equivalent copolymers, except for the HDDA Kelvin lattices, which were comparable. The HEMA IPN octet lattice had the highest energy dissipation ratio at 74.71 ± 0.50%. For the gradient-IPN lattices, the incorporation of HEMA resulted in higher energy dissipation ratios than HDDA lattices, for both Kelvin and octet lattices. However, the copolymer lattices benefitted more from HDDA than HEMA. This was likely due to small fractures forming in the stiffer HDDA shell of the gradient-IPNs (see below for more details) and affecting recovery in addition to stiffer copolymer lattices having improved recovery. Overall, all lattices fully recovered their original shape after cyclic compression tests with no noticeable fractures and residual strains less than 11%. The gradient-IPN lattices have a unique combination of high toughness, high energy absorption efficiency, and recoverability.

To further demonstrate recoverability beyond a singular compression, lattices were subjected to sequential cyclic compression tests with increasing strain values in increments of 10% strain (Figures S19,S20, and Table S8, Supporting Information). The Kelvin and octet lattices made of elastomeric polyurethane again showed minimal hysteresis loops from the compression loading-unloading curves with no obvious change upon increasing strain and all energy dissipation ratios below 33% (Figure S19a,b, Supporting Information). As evidenced by the higher energy dissipation ratios compared to the polyurethane lattices, the copolymer and gradient-IPN lattices displayed more pronounced hysteresis loops (Figure S19c–j, Supporting Information). The HEMA IPN lattices displayed higher energy dissipation ratios at all strain values compared to the HDDA IPN lattices. Fractures forming in the stiffer, highly crosslinked HDDA shell of the gradient-IPN upon successive compressive stress applied likely resulted in permanent deformations in the Kelvin HDDA IPN lattices. This hypothesis can be seen by more significant drops in the initial peak stress (estimated as the specific stress at 10% strain) between the 10% and 50% strain cycles for the HDDA IPN lattices compared to the HEMA IPN lattices (≈50% vs ≈25% drop, Figure S20, Supporting Information) as well as more jagged stress–strain curves upon successive compression (Figure S19i,j, Supporting Information). However, the HDDA IPN lattices recovered 93–96% of the original height after 50 % strain loading (Table S8, Supporting Information). On the other hand, HEMA IPN lattices had smaller drops in initial peak stress, indicating less microfracture formation and improved recoverability of the lattices, likely due to HEMA forming a linear polymer. The presence of some differences in cyclic compression curves of the HEMA IPN lattices with increasing strain levels could have been due to the polymer chains deforming elastically during compression at the same time that slippage (viscous deformation) occurred between polymer chains,[37] i.e., between the polyurethane and HEMA polymer in the gradient-IPN. During unloading, the elastic deformation of the polymer chains recovered instantly, but the slippage required more time to recover,[37] which caused the lower stress. Compared to the copolymer lattices, the gradient-IPN lattices exhibited both high toughness and high energy dissipation ratios, while the copolymer lattices had high energy dissipation ratios, but lower overall toughness. This was due to the copolymer lattices exhibiting lower overall initial peak stresses compared to the gradient-IPN lattices. In addition, the copolymer lattices had significant drops in stiffness and initial peak stress between the 10% and 50% strain curves (Figure S20, Supporting Information), despite not having a brittle outer shell, which led to deceptively high energy dissipation ratios, but lower energy absorption (for example, HDDA octet copolymer lattice in Figure S19h, Supporting Information between 40% and 50% strain cycles). While drops in stress occurred for all lattices between compression cycles, the recoverability could be improved with optimization of the experiment design (i.e., longer time between compression cycles to allow for polymer chain slippage recovery), particularly for the lattices that did not exhibit fracture formation. All of the gradient-IPN lattices recovered their original shape and can be tuned with lattice type, amount of stiff polymer (thickness of IPN shell), and type of material. The HEMA IPN lattice in particular is promising for energy dissipation due to its high toughness and recoverability. While the HDDA IPN lattices have higher toughness, the stiff IPN shell results in more fracture formation and, thus, lower recoverability. However, because of its higher toughness while still benefitting from the viscoelastic core, the HDDA IPN lattices could be useful for structural applications (e.g., vibration damping). Furthermore, the gradient-IPN core–shell morphology prevented catastrophic fracture with many of the lattices (those with thinner IPN shells) recovering their original shape, unlike the core–shell structures printed via extrusion-based 3D printing techniques with poor interfacial bonding between the multiple materials.[7,23]

3. Conclusion

A gradient polymer morphology consisting of a soft elastomeric core and stiff IPN shell was introduced into 3D printed lattices and resulted in enhanced and highly tunable energy absorption under compressive forces. The post-processing method used to incorporate gradient polymers and material properties into lattices can be adjusted to the desired stress–strain response. This work showed the tunability through the thickness of the stiff IPN shell (swelling time), type of stiff polymeric material in the gradient-IPN (linear HEMA and highly crosslinked HDDA polymers), degree of cure of the stiff polymer, and lattice geometry (Kelvin and octet unit cells). All of these handles can be used to yield superior properties relative to structures with equivalent material compositions without a polymer gradient and core–shell structure. In particular, the toughness at densification and stiffness increased by factors as high as 4 and 6, respectively, compared to copolymers without polymer gradients in the struts of 3D printed lattices. Cyclic compression tests showed excellent recoverability of the IPN lattices, particularly with the optimal choice of polymer material forming the gradient (e.g., HEMA). The benefits of this soft core-stiff shell structure are highlighted under compressive forces due to the combination of viscoelasticity enabling recoverability and load-bearing capabilities promoting buckling at higher stresses, all without a fracturing issue at the interface between the multiple materials. These properties were in contrast to tensile performance; thus, the optimization of materials for energy absorption must include evaluation of both the material and 3D geometry and not rely on using traditional materials testing methods. Kelvin IPN lattices with HEMA in the stiff shell showed the combined benefits of high toughness and recoverability, ideal for energy dissipation for impact protection, such as helmet liners, protective equipment, automotive crash absorbers, etc. HDDA IPN octet lattices had the highest toughness, but lower recoverability, which could be suitable for structural applications where the benefits of the viscoelastic core are required, but recoverability is not as important (e.g., vibration damping). This wide range of energy absorption applications is possible with this robust gradient-IPN method where the benefits exist across all lattice types, sizes, relative densities, etc. while having high control over tuning the properties. Both the material location (lattice architecture) and properties (gradient-IPN core–shell structure) can be altered to enhance performance.

There are three main key advantages to fabricating gradient-IPN morphology in the form of a stiff shell-soft core within 3D printed lattices: the simple, scalable, and cost-effective process; the versatility in parameters to tune the properties; and enhanced mechanical properties. The swelling, drying, and curing steps of incorporating a gradient-IPN into 3D printed structures are very similar to the typical wash, dry, and cure post-processing steps of vat photopolymerization techniques and can be readily applied to other 3D printed objects. The process is also highly versatile, both in terms of chemistry and applications. There is the potential for even more tunability beyond what is described in this report, including varying the crosslinking density and material gradient throughout the lattice structure (e.g., sharp vs gradual transitions in polymers), different types of crosslinking strategies (e.g., physical, covalent, etc.), different types of polymers (e.g., epoxides, thermal curable polymers, etc.), and, of course, many more lattice designs. All of these approaches can be altered and optimized to achieve the ideal energy absorber for the desired application with enhanced toughness compared to non-gradient materials. Therefore, this IPN method presents a powerful approach to incorporate multiple materials into vat photopolymerization 3D printing structures and could be expanded to integrate a wide range of material properties into 3D objects, such as gradients in hydrophobicity, hydrophilicity, resilience to biodegradation, thermal conductivity, refractive index, corrosion protection, noise damping, and others.

4. Experimental Section

Photoresin Preparation and Materials: The Ebecryl 8413 and Ebecryl 113 were provided by Allnex. The other monomers used were isobornyl acrylate (contains 200 ppm monomethyl ether hydroquinone as an inhibitor, technical grade, Sigma-Aldrich Canada Co.), HEMA (contains ≤250 ppm monomethyl ether hydroquinone as an inhibitor, 97%, Sigma-Aldrich Canada Co.) and HDDA (99% stab., Thermo Scientific). The photoinitiator was ethyl (2,4,6-trimethylbenzoyl) phenylphosphinate (TPO-L, Oakwood Products, Inc.). Fluorescein isothiocyanate isomer I (FITC, ≥90%, Sigma-Aldrich Canada Co.) was used as the fluorescent dye for microscopy images. Ethanol (95% vol., Commercial Alcohols by Greenfield Global) was used for washing the samples after printing, unless otherwise stated.

All photoresins contained 1 wt.% (weight percent) photoinitiator and 99 wt.% monomer(s). The components of each photoresin are described in Table S9 (Supporting Information). The weight ratio of monomers in the polyurethane photoresin was 5:5:1 Ebecryl8413:Ebecryl113:isobornyl acrylate. Each photoresin was mixed using a planetary centrifugal mixer (THINKY ARE-310). The polyurethane and copolymer photoresins were mixed for 10 min at 2000 rpm followed by defoaming (removes most air bubbles) for 30 s at 2200 rpm. The stiff polymer photoresins (with much lower viscosities) were mixed for 2 min at 2000 rpm followed by defoaming for 30 s at 2200 rpm. The photoresins were wrapped in aluminum foil and stored at 4 °C until use. Before use, the mixture was brought to room temperature by mixing for 2 min at 2000 rpm followed by defoaming for 30 s at 2200 rpm.

For the stiff polymer photoresins with fluorescent dye, the fluorescent dye stock solution was first prepared by dissolving fluorescein isothiocyanate isomer I (FITC) in anhydrous ethanol at a concentration of 15 mg mL^{-1} with 5 min of sonication (Cole-Parmer). Then 6.7 wt.% of FITC stock solution was combined with 93.3 wt.% of premixed HEMA or HDDA stiff polymer photoresins using a vortex mixer (G560, Cole–Parmer Scientific Industries) for 1 min. The FITC-photoresin was wrapped with aluminum foil and stored in the fridge at 4 °C until use. Before being used, the mixture was brought back to room temperature using the same 2 min at 2000 rpm and 30 s defoaming at 2200 rpm mixing procedure with the planetary mixer as described above.

The copolymer photoresin compositions were determined from the weight percent of the polyurethane and stiff polymer materials from the IPN 3D printed structures (see Table S9, Supporting Information for exact wt.%). Premixed polyurethane and stiff polymer photoresins were combined in the same weight ratio and mixed using a planetary mixer for 10 min at 2000 rpm followed by defoaming for 30 s at 2200 rpm. For example, if the equivalent IPN was 15 wt.% HEMA, 15 wt.% HEMA stiff polymer photoresin was combined with 85 wt.% polyurethane photoresin to create the copolymer photoresin.

3D Printing: An Asiga Max X27 UV385 Digital Light Processing (DLP) printer with a 385 nm light emitting diode (LED) light source was used for printing all lattices and rod samples. The samples were printed using a light intensity of 25 mW cm^{-2}, a slice thickness of 0.100 mm, exposure time of 1.938 s, burn-in (initial layers) exposure time of 15.684 s, one burn-in layer, and heater temperature set to 30 °C to warm the photoresin in the 1 L build tray. For the HEMA copolymer, the exposure time was set to 10.000 s with two burn-in layers. The printed objects were immersed in ethanol and sonicated for 10 min in order to remove residual uncured photoresin. The washing step was repeated twice more with new ethanol replenished in between. The washed samples were dried for 24 h in the air, then postcured with 1000 UV flashes in an Otoflash G171 UV light flash cure box (300 to 700 nm light) with nitrogen atmosphere purge. These curing conditions were kept the same for all 3D printed lattices and rods, including homopolymer (polyurethane, HDDA, and HEMA) and copolymer samples. For polyurethane and copolymer lattices, the flash curing method was used as constant curing (at a specific temperature at time) resulted in an undesirable decrease in the toughness of the polyurethane polymer and the lattice remained tacky. For lattices and rods printed with HDDA and HEMA, the washing step in ethanol was skipped and the samples were left for 24 h in air before curing with the Otoflash.

Details and images of the models of the lattices for mechanical testing and rod samples for other characterization are described in the Supporting Information Section (Table S10, Supporting Information). Cylindrical rods were chosen as the testing structure for swelling and tensile tests to more closely mimic the 3D lattice struts and degree of IPN incorporation as well as to evaluate the properties of a similar IPN morphology (cylindrical core–shell structure). For the scaled elastomeric and copolymer lattices, the scaling factor was determined from the average percent difference in dimensions between the actual as-printed IPN and elastomeric or copolymer lattices, which was then applied to the model before printing. The elastomeric and copolymer lattices printed with the scaled model resulted in a similar overall volume to the IPN and minimal change in density (see Table S6, Supporting Information), calculated by the difference in density (actual mass divided by the outer dimensions of the lattice) between the scaled and original unscaled lattice.

IPN Formation: After printing and post-processing the 3D-printed polyurethane, the stiff polymer photoresin was placed in a container, with enough volume to cover the 3D-printed polyurethane sample. The 3D printed polyurethane sample was submerged into the stiff polymer photoresin and placed on an orbital shaker (Thermo Scientific multi-purpose rotator) at speed 6 for the desired time as described in the Supporting Information Tables. The majority of samples were swelled for 15 min, unless varied for the swelling experiments or to achieve a desired wt.% stiff polymer for the samples (i.e., tensile tests). After swelling, the sample was removed and excess photoresin was removed by dabbing with a paper towel, shaking the sample in a paper towel, and drying with an air gun over all sides of the sample. The sample was then cured with either a Formlabs Form Cure box (405 nm light) at constant temperature and time or with 1000 UV flashes with the Otoflash. The lattices were placed in the center of the cure box to maintain a similar distance from the UV source. The curing conditions for HEMA and HDDA secondary polymers were optimized for each material (see Results and Discussion Section) and were as follows (unless otherwise stated): Formlabs Form Cure box at 45 °C for 60 min for HEMA stiff polymer photoresin swelled samples and 65 °C for 60 min for HDDA stiff polymer photoresin swelled samples. The same steps were followed for the fluorescence microscopy samples, except the stiff polymer photoresin with fluorescent dye mixture was used as the swelling photoresin.

The mass before and after IPN formation was compared to determine the wt.% of the stiff polymer in the 3D printed samples using the following Equation (1):

$$\mathit{wt\ \%\ stiff\ polymer}\quad (\%) = \frac{\mathit{mass\ of\ IPN} - \mathit{mass\ of\ polyurethane}}{\mathit{mass\ of\ IPN}} \times 100\% \tag{1}$$

The length and diameter of the cylindrical rods were compared before and after IPN formation to determine the percent change in dimensions and were calculated using the following Equation (2):

$$\mathit{Length\ /Diameter\ Percent\ Change}\quad (\%) = \frac{\mathit{IPN\ length/diameter} - \mathit{polyurethane\ length/diameter}}{\mathit{polyurethane\ length/diameter}} \times 100\% \tag{2}$$

The cylindrical rods for swelling tests were averaged over three rod samples. A total of three to five samples for each type of polymer (homopolymer, IPN, copolymer) were used for tensile tests and averaged.

Fluorescence Microscopy: Rectangular rods were chosen for fluorescence microscopy measurements in order to enable easier imaging of the cross-section of the IPN samples. The samples for fluorescent imaging were prepared by cutting each IPN sample into five blocks. The fluorescence microscopy images were captured by scanning each cross-section of the block on an inverted microscope (IX81, Olympus Life Science) using a high-resolution CCD Camera (CoolSNAP, Photometrics, USA), a 4×/0.10NA (Olympus Life Science) objective lens, and FITC optical filter (EX 485/20, EM 522/24, FF 506, Semrock). With a 120 W fluorescence light source set to 100% output power (X-Cite 120PC, Excelitas Technologies), the exposure time was set as 300 ms for HEMA IPN samples and 900 ms for HDDA IPN samples using InVitro microscope automation software (Media Cybernetics). To provide a measurement for the thickness of the IPN shell independent of the thickness of the overall IPN sample, a ratio of the thickness of the IPN shell (fluorescent region of the sample or diffusion length) to the thickness of the entire IPN sample along the short length of each cross-section were measured using ImageJ software on IPN samples after swelling and curing (see Figure S21, Supporting Information for an example). These values were used to calculate the percent diffusion using the following Equation (3):

$$\mathit{Percent\ Diffusion}\quad (\%) = \frac{\mathit{Diffusion\ length}\ \ (\mu m)}{\mathit{Sample\ thickness}\ \ (\mu m)} \times 100\% \tag{3}$$

The percent diffusion was averaged over ten measurements for each cross-section, two to four cross-sections for each sample, and one to two samples for each condition (20–80 measurements per IPN type).

Tensile Tests: The cylindrical rods were characterized mechanically based on a modification of the ISO-527-2 standard, using specimen dimensions inspired by configuration 1BB. The choice of rods over the standard dogbone shape was made to ensure uniformity of the IPN penetration during swelling. Testing procedures followed from the ISO standard, and measured their elastic modulus, ultimate tensile strength (UTS), toughness, and percent elongation via quasi-static tensile tests. An MTS Criterion C41 Table Top tensile machine with a load capacity of 1 kN was used to conduct tensile tests. All of the specimens were tested at a rate of 5 mm min^{-1} with the exception of the polyurethane homopolymer, and HEMA copolymer and IPN cylindrical rods which were tested at 50 mm min^{-1}. A load cell with 1000 N capacity was used to measure the force during the experiment. The crosshead motion was used to measure the displacement with an accuracy within ± 0.5%. The distance between the grips was adjusted at 15.1 mm. Pneumatic grips were used, applying a gripping pressure of 0.13 MPa to mount the specimens, followed by applying a pressure ranging between 0.41 to 0.55 MPa during the test. Stress was calculated using the actual cross-sectional area of the rods as measured using calipers before testing. Figure S22 (Supporting Information) displays a picture of the setup, showing the pneumatic grips and the specimen. Young's modulus was calculated as the stress–strain slope between 0.05 and 0.75% strain.

Compression Tests: The compression tests were performed using a Universal Testing Machine (INSTRON 5900R) with a 500 N or 5 kN load cell for all samples (the 5 kN load cell was used for the HDDA homopolymer lattices and HDDA IPN lattices swelled for 60 min). The compression tests were performed at 10 mm min^{-1} using the setup displayed in Figure S23 (Supporting Information). Stress–strain curves for each lattice sample were plotted using stress relative to the density (lattice mass divided by volume from the lattice outer dimensions), referred to as specific stress, to account for the change in mass and dimensions of the IPN samples. Energy absorption efficiency (η) was calculated to evaluate the ability of the lattice to absorb energy compared to an "ideal" energy absorber. This "ideal" energy absorption is impossible in reality as it requires infinite stiffness, followed by a perfectly horizontal stress plateau, and densification at a strain of 1.[38,39] The energy absorption efficiency was calculated using the Equation (4):

$$\eta = \frac{\int_0^{\varepsilon} \sigma d\varepsilon}{\sigma_{tr}} = \frac{T}{\sigma_{tr}} \tag{4}$$

where ϵ is the strain, σ is the stress, and σ_{tr} is the maximum transmitted stress up to strain ϵ. Energy absorption efficiency can also be measured from the ratio of toughness (area under the curve, T) to the maximum transmitted stress experienced up to a given strain, ϵ, for each strain value measured. The maximum energy absorption efficiency indicates the point (strain) at which the lattice densifies and any further increase in absorbed energy is less than the corresponding increase in stress. The densification strain is calculated from the strain at the maximum energy absorption efficiency.[40,41] Toughness at densification is the toughness calculated up to the densification strain. The photos and videos were recorded using a Nikon D7500 camera (≈60 frames s^{-1}).

Cyclic Compression Tests: Cyclic compression tests were performed with the same Universal Testing Machine and 500 N load cell. Two types of cyclic compression tests were performed. In the first test, the sample was preloaded to 0.1 N then compressed at room temperature to 40% strain followed by immediate (no pause) unloading to the zero point. The rate of loading and unloading was performed at 10% min^{-1}. In the second test, the sample was preloaded to 0.1 N then compressed at room temperature to different strain levels in each cycle ranging from 10% to 50% with a 10% increment (i.e., 5 cycles total). The same rate as the first test (10% min^{-1}) was used with no pause between loading and unloading. After unloading for each cycle, the test sample remained on the compression plates for 10 min to allow for recovery. The stress–strain curves of each loading and unloading cycle were recorded. The areas enclosed by the loading and unloading curves A_{load} and A_{unload}, respectively, were obtained by integrating the curves. The energy dissipation ratio was calculated using the following Equation (5):

$$\textit{Energy dissipation ratio} \quad (\%) = \frac{A_{load} - A_{unload}}{A_{load}} \times 100\% \tag{5}$$

Residual strains were determined as the strains between the loading and unloading curves when the stress reached zero. The reported mechanical properties from cyclic compression tests of the lattices were averaged over two samples.

Supporting Information

Supporting Information is available from the Wiley Online Library or from the author.

Acknowledgements

The authors thank Allnex, U.S.A. for kindly providing the Ebecryl 8413 and Ebecryl 113 monomers.

Open access funding provided by the National Research Council Canada library.

Conflict of Interest

The authors declare no conflict of interest.

Data Availability Statement

The data that support the findings of this study are available from the corresponding author upon reasonable request.

Keywords

3D printing, digital light processing, energy absorption, gradient materials, interpenetrating polymer network, lattices

Received: April 11, 2024
Revised: June 17, 2024
Published online:

[1] A. Orth, D. Webber, Y. Zhang, K. L. Sampson, H. W. de Haan, T. Lacelle, R. Lam, D. Solis, S. Dayanandan, T. Waddell, T. Lewis, H. K. Taylor, J. Boisvert, C. Paquet, *Nat. Commun.* **2023**, *14*, 4412.
[2] R. Hensleigh, H. Cui, Z. Xu, J. Massman, D. Yao, J. Berrigan, X. Zheng, *Nat. Electron.* **2020**, *3*, 216.
[3] J. J. Schwartz, A. J. Boydston, *Nat. Commun.* **2019**, *10*, 791.
[4] A. Velasco-Hogan, J. Xu, M. A. Meyers, *Adv. Mater.* **2018**, *30*, 1800940.
[5] S. Gantenbein, K. Masania, W. Woigk, J. P. W. Sesseg, T. A. Tervoort, A. R. Studart, *Nature* **2018**, *561*, 226.
[6] Y. Yang, X. Li, M. Chu, H. Sun, J. Jin, K. Yu, Q. Wang, Q. Zhou, Y. Chen, *Sci. Adv.* **2019**, *5*, eaau9490.
[7] J. Mueller, K. Shea, *Extrem. Mech. Lett.* **2018**, *25*, 7.
[8] L. R. Meza, S. Das, J. R. Greer, *Science* **2014**, *345*, 1322.
[9] N. A. Traugutt, D. Mistry, C. Luo, K. Yu, Q. Ge, C. M. Yakacki, *Adv. Mater.* **2020**, *2000797*, 1.
[10] C. Luo, C. Chung, N. A. Traugutt, C. M. Yakacki, K. N. Long, K. Yu, *ACS Appl. Mater. Interfaces* **2021**, *13*, 12698.
[11] E. C. Clough, T. A. Plaisted, Z. C. Eckel, K. Cante, J. M. Hundley, T. A. Schaedler, *Matter* **2019**, *1*, 1519.
[12] J. Brennan-Craddock, D. Brackett, R. Wildman, R. Hague, *J. Phys. Conf. Ser.* **2012**, *382*, 012042.
[13] R. F. P. Junio, P. H. P. M. da Silveira, L. de Mendonça Neuba, S. N. Monteiro, L. F. C. Nascimento, *Eng.* **2023**, *4*, 903.
[14] P. Zochowski, M. Bajkowski, R. Grygoruk, M. Magier, W. Burian, D. Pyka, M. Bocian, K. Jamroziak, *Metals (Basel)* **2021**, *11*, 1.
[15] C. Boursier Niutta, R. Ciardiello, A. Tridello, *Polymers (Basel)* **2022**, *14*, 1116.
[16] F. N. Habib, P. Iovenitti, S. H. Masood, M. Nikzad, *Mater. Des.* **2018**, *155*, 86.
[17] A. E. Gongora, L. Kelsey, R. Pang, T. J. Lawton, F. Elise, K. A. Brown, A. E. Gongora, K. L. Snapp, R. Pang, T. M. Tiano, K. G. Reyes, E. Whiting, T. J. Lawton, E. F. Morgan, K. A. Brown, *Matter* **2022**, *5*, 2829.
[18] J. Mueller, K. H. Matlack, K. Shea, C. Daraio, *Adv. Theory Simulations* **2019**, *2*, 1900081.
[19] L. Ren, Z. Wang, L. Ren, Z. Han, Q. Liu, *Compos. Part B* **2022**, *242*, 110086.
[20] K. U. Claussen, T. Scheibel, H. W. Schmidt, R. Giesa, *Macromol. Mater. Eng.* **2012**, *297*, 938.
[21] R. O. Ritchie, *Nat. Mater.* **2011**, *10*, 817.
[22] M. Rafiee, F. Granier, D. Therriault, *Adv. Mater. Technol.* **2021**, *6*, 1.
[23] J. Mueller, J. R. Raney, K. Shea, J. A. Lewis, *Adv. Mater.* **2018**, *30*, 1.
[24] D. Yavas, Q. Liu, Z. Zhang, D. Wu, *Mater. Des.* **2022**, *217*, 110613.

[25] K. L. Sampson, B. Deore, A. Go, M. A. Nayak, A. Orth, M. Gallerneault, P. R. L. Malenfant, C. Paquet, *ACS Appl. Polym. Mater.* **2021**, *3*, 4304.
[26] B. Deore, K. L. Sampson, T. Lacelle, N. Kredentser, J. Lefebvre, L. S. Young, J. Hyland, R. E. Amaya, T. Jamshid, P. R. L. Malenfant, H. W. de Haan, C. Paquet, *Nat. Commun.* **2021**, *12*, 55.
[27] Z. Xu, C. S. Ha, R. Kadam, J. Lindahl, S. Kim, H. F. Wu, V. Kunc, X. Zheng, *Addit. Manuf.* **2020**, *32*, 101106.
[28] L. H. Sperling, in *Interpenetr. Polym. Networks*, American Chemical Society, Washington, DC **1994**, pp. 1–3.
[29] S. Hong, D. Sycks, H. F. Chan, S. Lin, G. P. Lopez, F. Guilak, K. W. Leong, X. Zhao, *Adv. Mater.* **2015**, *27*, 4035.
[30] K. Bootsma, M. M. Fitzgerald, B. Free, E. Dimbath, J. Conjerti, G. Reese, D. Konkolewicz, J. A. Berberich, J. L. Sparks, *J. Mech. Behav. Biomed. Mater.* **2017**, *70*, 84.
[31] M. Caprioli, I. Roppolo, A. Chiappone, L. Larush, C. F. Pirri, S. Magdassi, *Nat. Commun.* **2021**, *12*, 2462.
[32] Y. S. Lipatov, L. V. Karabanova, *J. Mater. Sci.* **1995**, *30*, 2475.
[33] D. K. Patel, A. H. Sakhaei, M. Layani, B. Zhang, Q. Ge, S. Magdassi, *Adv. Mater.* **2017**, *29*, 1.
[34] L. V. Karabanova, S. V. Mikhalovsky, A. W. Lloyd, *J. Mater. Chem.* **2012**, *22*, 7919.
[35] V. S. Deshpande, M. F. Ashby, N. A. Fleck, *Acta Mater.* **2001**, *49*, 1035.
[36] P. Lin, S. Ma, X. Wang, F. Zhou, *Adv. Mater.* **2015**, *27*, 2054.
[37] P. Steindl, H. Decker, B. Retzl, Q. Jiang, A. Menner, A. Bismarck, *Polymer (Guildf)* **2021**, *215*, 123380.
[38] S. R. G. Bates, I. R. Farrow, R. S. Trask, *Mater. Des.* **2016**, *112*, 172.
[39] M. Avalle, G. Belingardi, R. Montanini, *Int. J. Impact Eng.* **2001**, *25*, 455.
[40] Q. M. Li, I. Magkiriadis, J. J. Harrigan, *J. Cell. Plast.* **2006**, *42*, 371.
[41] P. Wang, F. Yang, G. Lu, Y. Bian, S. Zhang, B. Zheng, H. Fan, *Compos. Part B Eng.* **2022**, *234*, 109724.